MIT Open Access Articles

CRISPR-mediated modeling and functional validation of candidate tumor suppressor genes in small cell lung cancer

The MIT Faculty has made this article openly available. ***Please share*** how this access benefits you. Your story matters.

Citation: Ng, Sheng Rong et al. "CRISPR-mediated modeling and functional validation of candidate tumor suppressor genes in small cell lung cancer." Proceedings of the National Academy of Sciences of the United States of America 117, 1 (January 2020): 513-521 ©2020 National Academy of Sciences.

As Published: http://dx.doi.org/10.1073/pnas.1821893117

Publisher: Proceedings of the National Academy of Sciences

Persistent URL: https://hdl.handle.net/1721.1/125148

Version: Final published version: final published article, as it appeared in a journal, conference proceedings, or other formally published context

Terms of Use: Article is made available in accordance with the publisher's policy and may be subject to US copyright law. Please refer to the publisher's site for terms of use.

CRISPR-mediated modeling and functional validation of candidate tumor suppressor genes in small cell lung cancer

Sheng Rong Ng[a,b], William M. Rideout III[a], Elliot H. Akama-Garren[a], Arjun Bhutkar[a], Kim L. Mercer[a,c], Jason M. Schenkel[a,d], Roderick T. Bronson[e], and Tyler Jacks[a,b,c,1]

[a]David H. Koch Institute for Integrative Cancer Research, Massachusetts Institute of Technology, Cambridge, MA 02139; [b]Department of Biology, Massachusetts Institute of Technology, Cambridge, MA 02139; [c]Howard Hughes Medical Institute, Massachusetts Institute of Technology, Cambridge, MA 02139; [d]Department of Pathology, Brigham and Women's Hospital, Boston, MA 02115; and [e]Department of Pathology, Tufts University School of Veterinary Medicine, North Grafton, MA 01536

Contributed by Tyler Jacks, November 19, 2019 (sent for review December 24, 2018; reviewed by Roman K. Thomas and Andrea Ventura)

Small cell lung cancer (SCLC) is a highly aggressive subtype of lung cancer that remains among the most lethal of solid tumor malignancies. Recent genomic sequencing studies have identified many recurrently mutated genes in human SCLC tumors. However, the functional roles of most of these genes remain to be validated. Here, we have adapted the CRISPR-Cas9 system to a well-established murine model of SCLC to rapidly model loss-of-function mutations in candidate genes identified from SCLC sequencing studies. We show that loss of the gene *p107* significantly accelerates tumor progression. Notably, compared with loss of the closely related gene *p130*, loss of *p107* results in fewer but larger tumors as well as earlier metastatic spread. In addition, we observe differences in proliferation and apoptosis as well as altered distribution of initiated tumors in the lung, resulting from loss of *p107* or *p130*. Collectively, these data demonstrate the feasibility of using the CRISPR-Cas9 system to model loss of candidate tumor suppressor genes in SCLC, and we anticipate that this approach will facilitate efforts to investigate mechanisms driving tumor progression in this deadly disease.

small cell lung cancer | CRISPR | GEMM | p107

SCLC is a highly aggressive neuroendocrine lung carcinoma that comprises around 13–15% of all diagnosed lung cancer cases (1). The disease is characterized by rapid growth and early widespread metastasis with the majority of patients presenting with extensive stage disease (2). Although SCLC patients often exhibit robust initial responses to cytotoxic chemotherapy, relapse almost invariably occurs, and no effective second-line therapies currently exist (3). Despite decades of research, few new therapies have demonstrated significantly improved outcomes for SCLC patients, in contrast to the growing number of options available for treating non-small cell lung cancer (4).

Genetically engineered mouse models (GEMMs) of SCLC have been used extensively to study the molecular mechanisms of tumor progression in SCLC. Based on the fact that inactivating mutations in the tumor suppressor genes *TP53* and *RB1* are found in almost all human SCLC tumors (5, 6), a murine model of SCLC (mSCLC) was developed by conditionally deleting *Trp53* and *Rb1* in the murine lung epithelium (7). This model faithfully recapitulates the key features of human SCLC, including histopathological appearance, expression of key neuroendocrine markers, and pattern of metastatic spread (7). Subsequent studies have utilized the *Trp53*/*Rb1* double knockout model of SCLC to functionally investigate additional genes, such as *Rbl2* (also known as *p130*), *Pten*, *Mycl1*, *Nfib*, *Myc*, and *Crebbp* (8–17).

Large-scale cancer genome sequencing studies have generated an extensive catalog of genes that are mutated in numerous cancer types (18). It remains a significant challenge to distinguish between driver and passenger mutations in order to identify genes or pathways that are truly important for tumor progression. This is particularly relevant in cancers that have high mutation rates, such as lung cancer (5, 19–21). One recent study involving SCLC identified multiple recurrently altered genes in these tumors, including inactivating mutations in the Notch signaling pathway, which was subsequently shown to functionally contribute to SCLC tumor progression (5). However, apart from a few other notable examples, many of the most frequently mutated genes have yet to be functionally validated in SCLC.

The development of the CRISPR-Cas9 system for genome editing in mammalian cells (22–24) has revolutionized the field of cancer research, enabling rapid validation of candidate oncogenes and tumor suppressor genes both in vitro as well as in vivo. This has been especially useful when combined with GEMMs of various cancers (25–32). By bypassing the need to generate new germline or conditional alleles for each gene of interest, the CRISPR-Cas9

Significance

SCLC is a deadly disease for which treatment outcomes have not improved significantly for over 30 y due to the lack of effective new therapies. Large-scale sequencing studies have identified many recurrently mutated genes in human SCLC tumors, whose functions remain poorly understood. We have adapted the CRISPR-Cas9 system to rapidly model mutations in target genes in a mouse model of SCLC. Using this system, we show that the gene *p107* functions as a tumor suppressor gene in SCLC. Furthermore, loss of *p107* confers a distinct tumor phenotype from loss of its close relative *p130*. Our results demonstrate the utility of our system for better understanding the genetic factors that contribute to SCLC progression.

Author contributions: S.R.N. and T.J. designed research; S.R.N., W.M.R., E.H.A.-G., and K.L.M. performed research; S.R.N., A.B., J.M.S., R.T.B., and T.J. analyzed data; and S.R.N. and T.J. wrote the paper.

Reviewers: R.K.T., University of Cologne; and A.V., Memorial Sloan Kettering Cancer Center.

Competing interest statement: T.J. is a member of the Board of Directors of Amgen and Thermo Fisher Scientific. He is also a co-founder of Dragonfly Therapeutics and T2 Biosystems. T.J. serves on the Scientific Advisory Board of Dragonfly Therapeutics, SQZ Biotech, and Skyhawk Therapeutics. None of these affiliations represent a conflict of interest with respect to the design or execution of this study or interpretation of data presented in this paper. Dr. Jacks's laboratory currently also receives funding from the Johnson & Johnson Lung Cancer Initiative and Calico, but this funding did not support the research described in this paper.

This open access article is distributed under Creative Commons Attribution-NonCommercial-NoDerivatives License 4.0 (CC BY-NC-ND).

Data deposition: The data reported in this paper have been deposited in the Gene Expression Omnibus (GEO), https://www.ncbi.nlm.nih.gov/geo, accession no. GSE139444. All other data generated or analyzed during this study are included in this published article, *SI Appendix*, and Datasets S1–S3.

[1]To whom correspondence may be addressed. Email: tjacks@mit.edu.

This article contains supporting information online at https://www.pnas.org/lookup/suppl/doi:10.1073/pnas.1821893117/-/DCSupplemental.

First published December 23, 2019.

Downloaded at MIT LIBRARIES on March 30, 2020

system has greatly increased the speed at which candidate genes, such as those identified from cancer genome sequencing studies or genetic screens, can be functionally validated in relevant preclinical models of cancer. These systems also streamline the development of in vivo models with which to examine the biological effects of multiple tumor-associated mutations.

In this study, we have adapted the CRISPR-Cas9 system to the *Trp53*/*Rb1* model of SCLC. We demonstrate the utility of this system to rapidly model loss of function of candidate tumor suppressor genes in SCLC. In particular, we show that loss of p107 (also known as Rbl1), a member of the retinoblastoma family of proteins that is recurrently mutated in a subset of human SCLC tumors (5), significantly accelerates tumor progression in the *Trp53*/*Rb1*-mutant background. Notably, loss of p107 appears to confer a distinct tumor phenotype compared with loss of p130, another member of the retinoblastoma family.

Results

Strategy for CRISPR-Mediated Targeting of Genes in mSCLC. We generated a Cre-activated allele of Cas9 targeted to the *Rosa26* locus (Fig. 1*A*). This allele also coexpresses EGFP and Csy4 (also known as Cas6f); the latter is a Type I CRISPR-Cas endonuclease that recognizes and cleaves RNA at a 28-nucleotide sequence (33) and has previously been used for multiplexed single guide RNA (sgRNA) expression from a single RNA transcript (34). We crossed this allele into the *Trp53*$^{flox/flox}$; *Rb1*$^{flox/flox}$ background to generate Trp53/Rb1/Cas9 animals. To allow for monitoring of tumor progression in vivo, we also crossed a Cre-activated luciferase reporter allele into these animals (9, 12).

To restrict CRISPR-Cas9 activity specifically to initiated tumor cells in vivo, we generated an adenoviral vector, Ad5-USEC (U6-sgRNA-EFS-Cre), that expresses a sgRNA targeting a gene of interest together with Cre recombinase (Fig. 1*B*). We chose to use an adenoviral vector instead of a lentiviral vector due to the observation that lentiviral-mediated tumor initiation frequently resulted in the broadening of the tumor spectrum in *Trp53*$^{flox/flox}$; *Rb1*$^{flox/flox}$ animals, including an increased rate of histiocytic sarcoma formation. Cre activity in the Ad5-USEC vector was validated in vitro using the Green-Go reporter cell line previously generated in our laboratory, in which GFP is activated upon Cre expression (27) (Fig. 1*C*). SCLC tumors were initiated by intratracheal administration of Ad5-USEC into the lungs of animals (35).

Loss of p107 Accelerates Tumor Progression in SCLC. To validate this system, we chose to target *p107* and *p130*, both of which are members of the retinoblastoma family of proteins that are recurrently mutated in around 6% of human SCLC tumors each (5). In particular, *p130* was chosen as a positive control because germline p130 conditional alleles have been previously used to accelerate tumor progression in SCLC (8). We designed sgRNAs targeting *p107* and *p130* and validated their activity in vitro in Green-Go cells that were transduced with a Cas9-expressing lentivirus (36), both by deep sequencing of the respective target genomic loci to assess the efficiency of generation of mutations (*SI Appendix*, Fig. S1*A*) as well as by Western blot to confirm a decrease in protein levels (*SI Appendix*, Fig. S1 *B* and *C*).

To test our system in vivo, we infected Trp53/Rb1/Cas9 animals with Ad5-USEC vectors expressing sgRNAs targeting *p107*, *p130*, or a control unannotated region of the genome (sgp107, sgp130, and control sg, respectively). At 5.5 mo posttumor initiation, we performed in vivo bioluminescence imaging to track tumor progression in these animals. We observed higher luciferase activity in both sgp130- and sgp107-infected animals compared with control animals (Fig. 2 *A* and *B*), consistent with a significant acceleration in tumor progression. Furthermore, both sgp130- (232 d) and sgp107-infected animals (205 d) showed decreased median survival compared with control animals (267 d; Fig. 2*C*). The acceleration of tumor progression that we observed in sgp130-infected animals recapitulates the results obtained in a previous

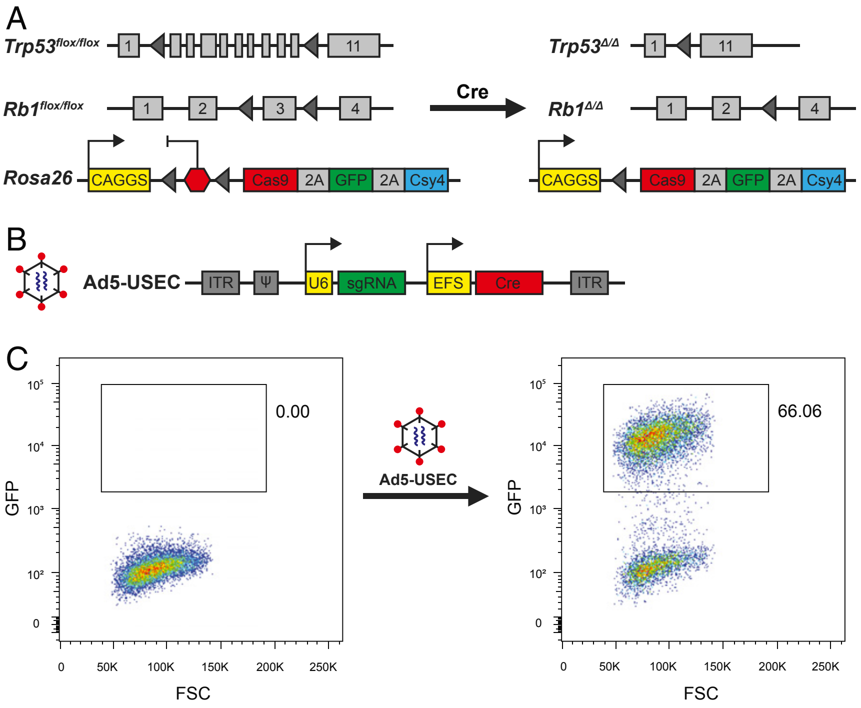

Fig. 1. Strategy for in vivo CRISPR-mediated targeting of genes in mSCLC. (*A*) Schematic of the Rosa26-CAGGS-LSL-Cas9-GFP-Csy4 allele crossed into the *Trp53/Rb1* double knockout model of SCLC. (*B*) Schematic of the Ad5-USEC vector. (*C*) In vitro validation of the Ad5-USEC vector in the Green-Go reporter cell line, which harbors a Cre-activated GFP cassette. Cells were analyzed by flow cytometry 4 d posttransduction.

Downloaded at MIT LIBRARIES on March 30, 2020

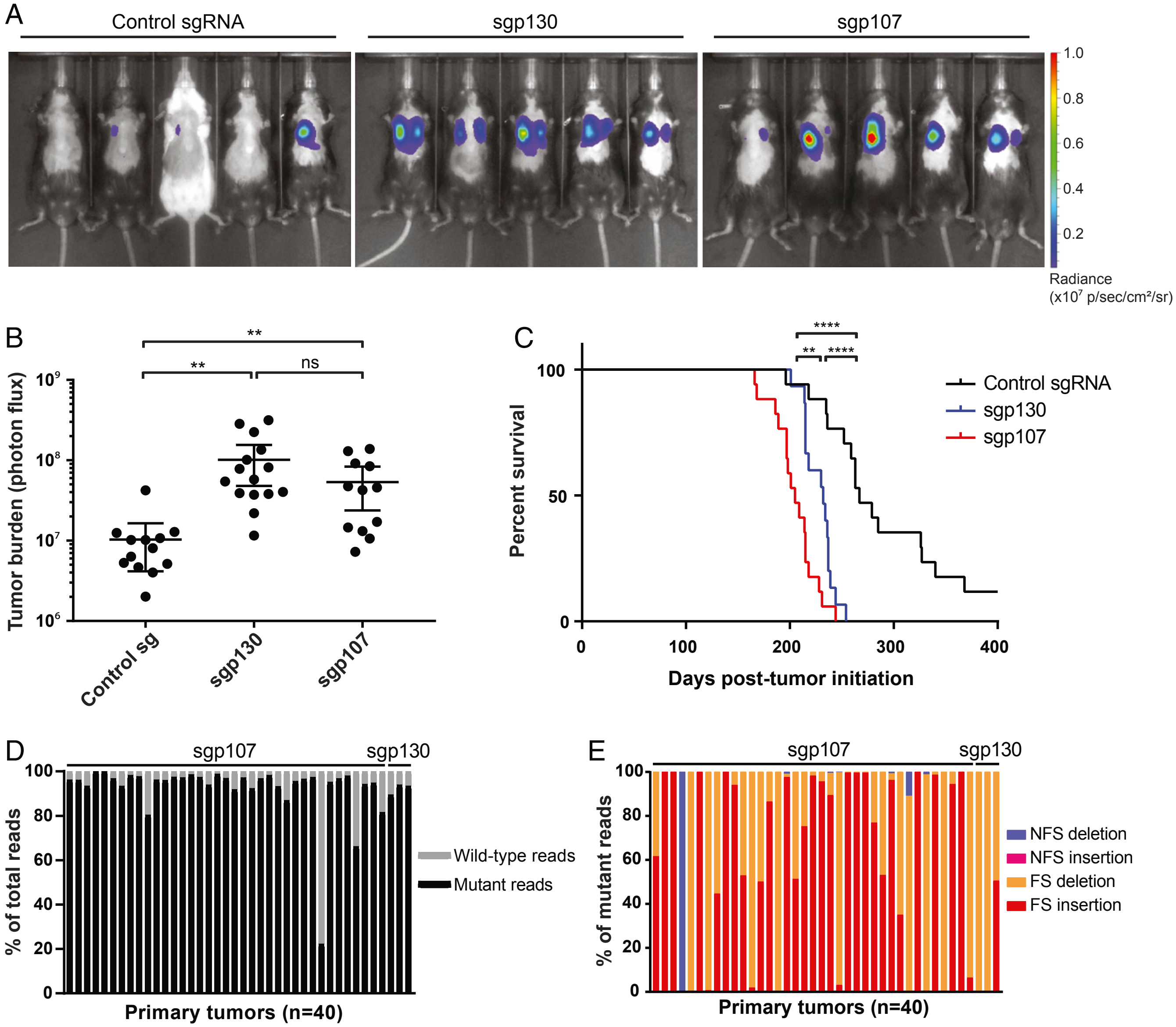

Fig. 2. Loss of p107 accelerates tumor progression in SCLC. (*A*) Representative images from in vivo bioluminescence imaging of Trp53/Rb1/Cas9 animals infected with Ad5-USEC harboring the indicated sgRNAs. Animals were imaged ~5.5 mo posttumor initiation. (*B*) Quantification of tumor burden in Trp53/Rb1/Cas9 animals infected with Ad5-USEC harboring control sgRNA ($n = 13$), sgp130 ($n = 15$), or sgp107 ($n = 13$) by in vivo bioluminescence imaging. Data are presented as means with error bars denoting 95% CI $**P < 0.005$, ns: not significant, 2-tailed Student's *t* test. (*C*) Survival analysis for Trp53/Rb1/Cas9 animals infected with control sgRNA ($n = 17$), sgp130 ($n = 15$), or sgp107 ($n = 17$). $**P < 0.005$, $****P < 0.0001$, log-rank (Mantel–Cox) test. (*D* and *E*) Deep sequencing of *p107* or *p130* genomic loci from tumors isolated from Trp53/Rb1/Cas9 animals infected with the respective sgRNAs, showing the proportion of mutant and wild-type sequencing reads (*D*), as well as the proportion of each indicated type of mutation for each tumor (*E*). FS: frameshift, NFS: nonframeshift.

study using conditional *Trp53/Rb1/p130* triple knockout SCLC mice (8).

To determine whether the observed phenotypes were a result of loss of *p130* or *p107* gene function, we isolated genomic DNA from tumors dissected from infected animals, then performed targeted deep sequencing of the genomic loci targeted by the respective sgRNAs. We observed that the vast majority of detected sequences contained either frameshift insertions or deletions (Fig. 2 *D* and *E* and *SI Appendix*, Fig. S2), with tumors harboring 1–4 different mutant alleles each. This result is consistent with a strong positive selection pressure for loss-of-function alleles in these tumors. Collectively, these data validate our approach for modeling loss-of-function mutations in this model and demonstrate that p107, like p130, is a functional tumor suppressor in SCLC.

Distinct Consequences of Loss of p107 and p130 in SCLC. To more closely examine changes in tumor progression upon loss of p107 or p130, we analyzed cohorts of infected Trp53/Rb1/Cas9 mice at fixed time points posttumor initiation. Analysis of hematoxylin and eosin (H&E)-stained lung sections from animals 6 mo posttumor initiation showed that loss of either p107 or p130 increases overall lung tumor burden compared with control animals (Fig. 3 *A* and *B*), consistent with our in vivo bioluminescence imaging result. In addition, there was no significant difference in tumor burden between sgp107- and sgp130-infected animals (Fig. 3*B*). However, there was a marked difference in the tumor phenotype observed in both groups of animals. sgp107-infected animals developed fewer tumors but with a larger mean tumor size, compared with sgp130-infected animals (Fig. 3 *C* and *D*).

Downloaded at MIT LIBRARIES on March 30, 2020

Importantly, these differences were also observed in animals analyzed at an earlier time point (4 mo posttumor initiation) when tumors were still relatively small and distinct (*SI Appendix*, Fig. S3 *A–D*). Because tumor numbers in both sgp130- and sgp107-infected animals were consistent between both time points (Fig. 3*C* and *SI Appendix*, Fig. S3*C*), we concluded that quantification of tumor number and size was not confounded by the collision of multiple independent tumors in late-stage animals.

Notably, sgp107-infected animals also displayed a greater incidence of mediastinal lymph node metastasis compared with sgp130-infected animals at this time point (Fig. 3*E*). This finding is consistent with the observation that sgp107-infected animals showed slightly reduced median survival compared with sgp130-infected animals despite similar lung tumor burden (Fig. 2*C*), as the mediastinal lymph node metastases likely accelerated the onset of breathing difficulties in these animals.

The differences between sgp130- and sgp107-infected animals prompted us to perform additional histological analyses. As expected, tumors that developed in all animals retained the characteristic histological features of SCLC, including positive immunohistochemical staining for the neuroendocrine markers Ascl1 and CGRP as well as heterogeneous staining for Hes1 (37) (Fig. 4*A*), confirming that the observed differences were not a result of a change in tumor spectrum. However, sgp130-infected animals frequently presented with numerous in situ tumors lining their major airways at 4 mo posttumor initiation, whereas far fewer in situ tumors were observed in sgp107-infected animals (Fig. 4 *B* and *C*). Overall, a higher fraction of tumors in sgp130-infected animals were in situ lesions rather than invasive tumors, compared with sgp107-infected animals (Fig. 4*D*). Therefore, loss of p107 results in an altered distribution of early tumor lesions within the lung compared with loss of p130, suggesting that p130 loss may lead to the transformation of a broader set of cells compared with p107 loss.

We also analyzed rates of proliferation and apoptosis in tumors from both sets of animals. Late-stage tumors from sgp107-infected animals displayed higher proliferation rates compared with tumors from sgp130-infected animals as measured by increased phosphorylated histone H3 (pHH3) staining (Fig. 4*E*). Interestingly, this difference was not observed in early-stage tumors (Fig. 4*E*). Conversely, sgp130 tumors displayed lower apoptosis rates compared with sgp107 tumors at both early and late stages as measured by decreased cleaved caspase-3 (CC3) staining (Fig. 4*E*). Collectively, these data demonstrate that p107 loss results in distinct consequences on SCLC development compared with loss of p130.

To gain insight into potential mechanisms underlying the distinct phenotypes observed between sgp107- and sgp130-infected animals, we performed RNA sequencing (RNA-seq) on multiple independent late-stage primary tumors isolated from infected animals (Dataset S1). We employed independent component analysis (ICA) (38), an

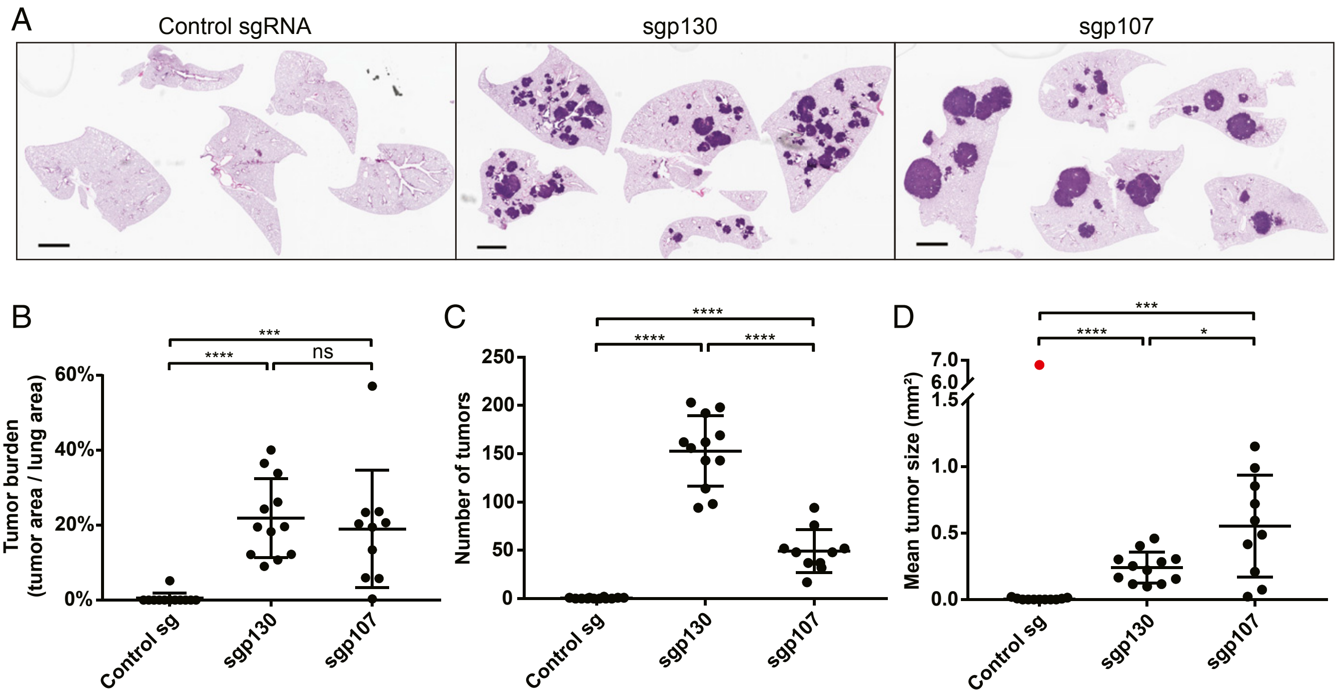

E

	Metastasis	No metastasis
Control sgRNA	0	12
sgp130	2	10
sgp107	7	3

ns
*
***

Fig. 3. Distinct consequences of loss of p107 and p130 on SCLC tumor progression. (*A*) Representative H&E-stained lung sections from Trp53/Rb1/Cas9 animals infected with Ad5-USEC harboring the indicated sgRNAs. Animals were analyzed 6 mo posttumor initiation. (Scale bars, 2 mm.) (*B–D*) Quantification of tumor burden (*B*), number of tumors (*C*), and mean tumor size (*D*) in Trp53/Rb1/Cas9 animals infected with Ad5-USEC harboring control sgRNA ($n = 12$), sgp130 ($n = 12$), or sgp107 ($n = 10$), 6 mo posttumor initiation. For (*D*), red indicates a data point that was identified as an outlier (Grubbs' test, $\alpha < 0.001$) and excluded from subsequent analyses. Data are presented as means with error bars denoting SD. ns: not significant, *$P < 0.05$, ***$P < 0.001$, ****$P < 0.0001$, 2-tailed Student's *t* test. (*E*) Quantification of the number of animals presenting with mediastinal lymph node metastasis upon necropsy at 6 mo posttumor initiation. ns: not significant, *$P < 0.05$, ***$P < 0.001$, 2-sided Fisher's exact test.

Downloaded at MIT LIBRARIES on March 30, 2020

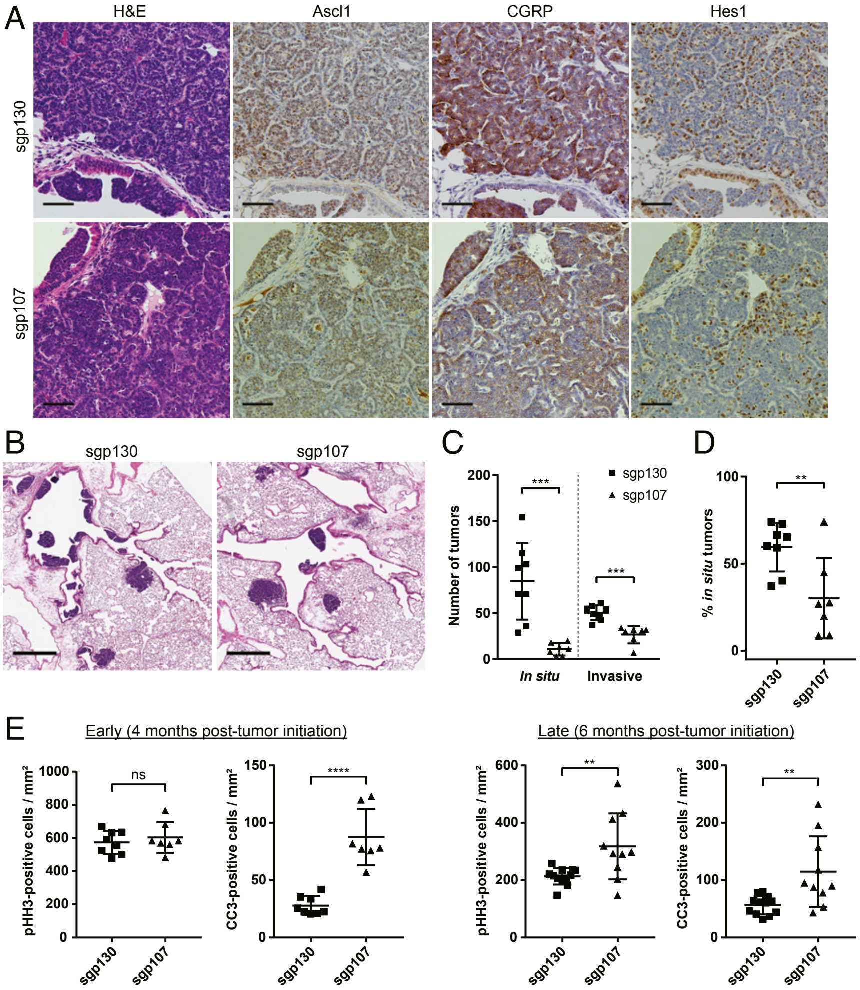

Fig. 4. Histological analysis of sgp130 and sgp107 tumors. (*A*) Representative H&E (first column) and IHC staining of serial sections of tumors from Trp53/Rb1/Cas9 animals infected with Ad5-USEC harboring the indicated sgRNAs. Tumors were stained for Ascl1, CGRP, or Hes1 as indicated. Animals were analyzed 4 mo posttumor initiation. (Scale bars, 50 μm.) (*B*) Representative H&E-stained sections of major airways in the lungs from Trp53/Rb1/Cas9 animals infected with Ad5-USEC harboring the indicated sgRNAs. Animals were analyzed 4 mo posttumor initiation. (Scale bars, 500 μm.) (*C* and *D*) Quantification of the number of in situ and invasive tumor lesions (*C*) as well as the overall percentage of in situ tumors (*D*) in Trp53/Rb1/Cas9 animals infected with Ad5-USEC harboring sgp130 ($n = 8$) or sgp107 ($n = 7$), 4 mo posttumor initiation. Data are presented as means with error bars denoting SD. $^{**}P < 0.005$, $^{***}P < 0.001$, 2-tailed Student's *t* test. (*E*) Quantification of pHH3-positive cells and CC3-positive cells per unit tumor area in Trp53/Rb1/Cas9 animals infected with Ad5-USEC harboring the indicated sgRNAs. Animals were analyzed 4 mo (*Left*) or 6 mo (*Right*) posttumor initiation. Data are presented as means with error bars denoting SD. ns: not significant, $^{**}P < 0.005$, $^{****}P < 0.0001$, 2-tailed Student's *t* test.

unsupervised blind source separation technique (see *Materials and Methods*), to generate gene expression signatures characterizing transcriptional profiles within this dataset (*SI Appendix*, Fig. S4*A* and Dataset S2). ICA was performed on autosomal genes as initial results indicated a dominant gender-specific signature within the dataset (reflecting a gender bias between sgp107- and sgp130-infected animals). A statistically significant signature that differentiated between sgp130 and sgp107 tumors was detected ($P = 0.0104$, Mann–Whitney *U* test) and further analyzed using gene set enrichment analysis (GSEA) (39). We observed an enrichment for several immune-related gene sets in sgp107 tumors (*SI Appendix*, Fig. S4*B* and Dataset S3). To validate this observation, we performed immunohistochemical staining of lung sections from late-stage animals for several immune markers—CD45, B220, and CD3. We observed tertiary lymphoid structure (TLS) formation in the lungs of both sgp107- and sgp130-infected animals (Fig. 5*A*). However, sgp107-infected animals harbored more TLS per tumor compared with sgp130-infected animals (Fig. 5*B*), even though there was no significant difference between the total number of TLS in each animal (*SI Appendix*, Fig. S5*A*). In particular, we observed an increase in intratumoral and peritumoral TLS, but not extratumoral TLS, in sgp107-infected animals compared with sgp130-infected animals (Fig. 5*C* and *SI Appendix*, Fig. S5*B*). Therefore, these data are consistent with the RNA-seq results and indicate an increase in immune cell infiltration in sgp107 tumors compared with sgp130 tumors.

Discussion

Functional studies in GEMMs have long been hampered by the need to generate new germline or conditional alleles for each new gene of interest. Approaches such as gene targeting in embryonic stem cells derived from GEMMs (11) have reduced the time needed to generate new mouse models but still require the dedication of significant time and resources. The ability of the CRISPR-Cas9 system to generate genomic alterations in somatic cells in vivo with high efficiency allows this process to be bypassed (40). In this study, we have demonstrated the feasibility of this approach in SCLC by modeling loss of p107 and p130 in the *Trp53*/*Rb1* double knockout model of SCLC, showing that loss of p107 significantly accelerates tumor progression to a similar

Downloaded at MIT LIBRARIES on March 30, 2020

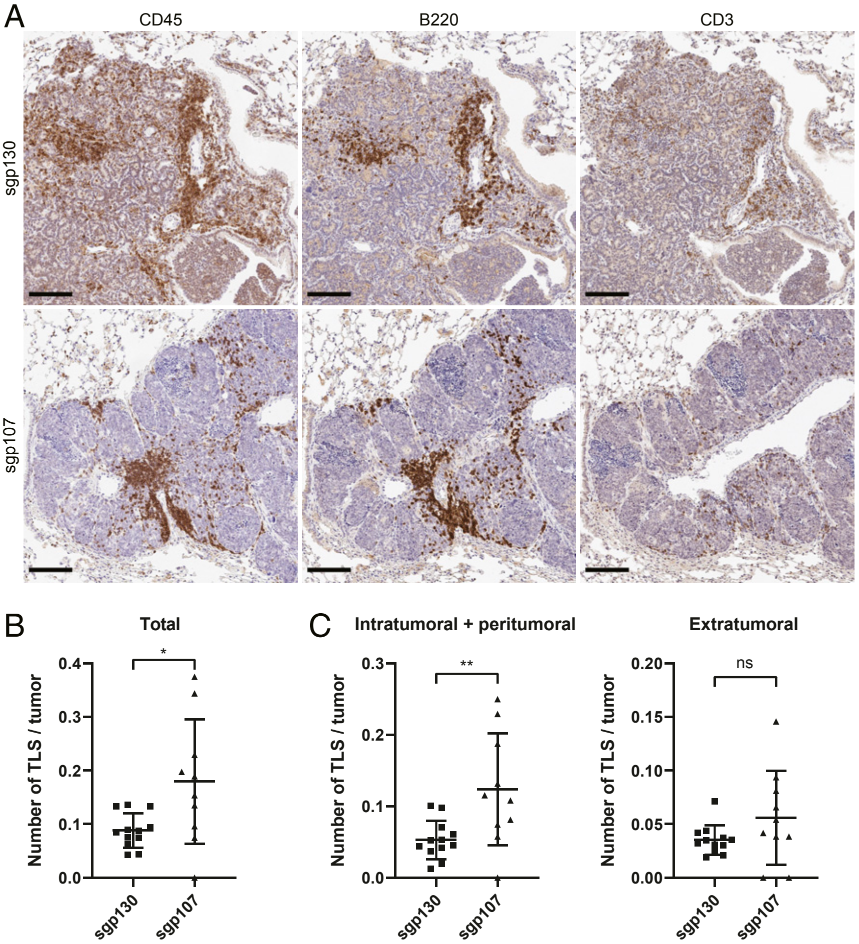

Fig. 5. Differences in TLS formation between sgp130- and sgp107-infected animals. (*A*) Representative IHC staining of serial sections of tumors from Trp53/Rb1/Cas9 animals infected with Ad5-USEC harboring the indicated sgRNAs. Tumors were stained for CD45, B220, or CD3 as indicated. Animals were analyzed 6 mo posttumor initiation. (Scale bars, 100 μm.) (*B*) Quantification of the total number of TLS in Trp53/Rb1/Cas9 animals infected with Ad5-USEC harboring sgp130 ($n = 12$) or sgp107 ($n = 10$), normalized to tumor number per animal. Animals were analyzed 6 mo posttumor initiation. (*C*) Quantification of number of intratumoral and peritumoral TLS (*Left*) or extratumoral TLS (*Right*), normalized to tumor number per animal in the same cohort of animals. Data in *B* and *C* are presented as means with error bars denoting SD. ns: not significant, $^{*}P < 0.05$, $^{**}P < 0.005$, 2-tailed Student's *t* test.

extent as loss of p130. However, we also observed several differences in tumor phenotype between p107-mutated and p130-mutated tumors, indicating potential biological differences between SCLC tumors with these genotypes.

CRISPR-mediated knockout of genes has been particularly useful for modeling loss-of-function mutations in tumor suppressor genes, such as those as demonstrated here, as well as in other models (25, 27, 30, 32). Other studies have demonstrated the ability to generate gain-of-function alterations, such as chromosomal rearrangements (26), as well as homologous recombination-mediated activation of oncogenes (25), albeit at a very low efficiency in the latter case. The adaptation of CRISPR-Cas9 for transcriptional activation or inhibition (41–46) has further extended the utility of the CRISPR-Cas9 system for modeling additional gain-of-function mutations. In particular, the ability to perform in vivo transcriptional activation using wild-type Cas9 has been reported (47). We expect that similar approaches will also be possible in SCLC using our system.

The use of autochthonous models of cancer, including SCLC, to study metastasis has led to key insights into the molecular determinants of metastatic spread (13, 48–50). In animals harboring multiple independent primary tumors, the use of barcoding techniques enables metastatic tumors to be matched to their respective seeding primary tumors, so as to distinguish primary tumors based on their metastatic potential (48, 49). By taking advantage of the imprecise repair of CRISPR-mediated double-stranded breaks in the cell by nonhomologous end joining, we observed that the different combinations of mutant alleles within each tumor could also be used as a barcode to match primary and metastatic tumors within the same animal (*SI Appendix*, Fig. S6). Although the use of single target sites, such as those presented in our study, may leave some ambiguity in matching metastatic tumors to primary tumors, the inclusion of additional sgRNAs targeting different genomic locations can significantly reduce this ambiguity; similar approaches have been used to trace cell lineages both in vitro and in vivo (51–53).

Due to the flexibility afforded by the CRISPR-Cas9 system, we were able to rapidly compare the effects of loss of p107 with loss of p130 in SCLC progression, which has not been performed previously. Both genes are mutated in about 6% of human SCLC tumors in a predominantly mutually exclusive fashion (5). We found that loss of p107 in the *Trp53*/*Rb1*-mutant background resulted in fewer but larger tumors compared with loss of p130. Furthermore, loss of p107 also accelerated the development of metastatic spread in these animals. These suggest that the 2 genes may play different roles in SCLC development, with loss of p130 appearing to promote tumor initiation and loss of p107 promoting tumor progression. p107 and p130 have been shown

Downloaded at MIT LIBRARIES on March 30, 2020

to exhibit different timings of expression and interaction with E2F family proteins during the cell cycle (54, 55), as well as to interact with different downstream effectors (56). p107 and p130 have also previously been reported to have distinct roles in lung epithelial development (57). Deletion of *Rb1* in the lung epithelium of *p107*$^{-/-}$ animals results in increased pulmonary epithelial proliferation in E18.5 embryos compared with deletion of *Rb1* in *p107*$^{+/+}$ animals, while having no effect on apoptosis. Conversely, deletion of *Rb1* in *p130*$^{-/-}$ animals results in decreased apoptosis but has no effect on proliferation. We demonstrate that p107 and p130 play similar roles in the context of SCLC development, with loss of p107 in SCLC tumors resulting in increased proliferation and loss of p130 resulting in decreased apoptosis. This provides a potential explanation for the observed differences in tumor phenotypes. Loss of p130 may allow for nascent transformed cells to escape apoptosis, resulting in an increase in the number of initiated tumors, whereas loss of p107 results in an increase in proliferation rate of developing tumors and, hence, larger tumor size without affecting tumor initiation.

In addition, we observed a difference in the number of tumor-associated TLS formed in the lungs of sgp107-infected animals compared with sgp130-infected animals. TLS represent sites of T and B cell priming and have been associated with a positive prognosis in many tumor types (58, 59). Previous work has demonstrated that TLS can be induced by several different cytokines, including IL-17, TNFα, and IL-6 (60). Collectively, the difference in tumor-associated TLS suggests that there are alterations to the inflammatory nature of the microenvironment in p130- and p107-mutant tumors and may indicate differences in the overarching antitumor immune response. Collectively, these alterations may have therapeutic implications, potentially influencing the response of these tumors to various types of immunotherapy, although more work will be needed to establish the relevance of this observation.

To summarize, we have demonstrated the feasibility of using the CRISPR-Cas9 system for modeling loss of tumor suppressor genes in an autochthonous mouse model of SCLC. This opens the door for rapid functional validation of other candidate genes of interest that are frequently mutated in SCLC. In addition, we anticipate that this approach, combined with ongoing advances in CRISPR-based tools for genetic and transcriptomic perturbations, as well as developments in the use of lentiviral vectors with in vivo models of SCLC (61), will also be useful for validation of therapeutic targets for SCLC in the future.

Materials and Methods

Animal Studies. All animal studies were approved by the MIT Institutional Animal Care and Use Committee. All mice were maintained on a mixed C57BL/6;129/Sv background. *Trp53*$^{flox/flox}$; *Rb1*$^{flox/flox}$; *Rosa26*$^{LSL\text{-}Luciferase/LSL\text{-}Luciferase}$ mice have been described previously (9, 12). Tumors were initiated by intratracheal delivery of 2×10^8 plaque-forming units of adenovirus expressing Cre recombinase as previously described (35). Animals were infected at ∼8–12 wk of age. Adenovirus stocks were prepared and titered as described below. For in vivo bioluminescence imaging, mice were anesthetized by isoflurane inhalation, administered with 150 mg/kg of D-luciferin (PerkinElmer #122799) by i.p. injection, then imaged 10-min postadministration using the IVIS Spectrum In Vivo Imaging System (PerkinElmer). Visualization and quantification of the bioluminescence signal was performed using Living Image (PerkinElmer).

For all animal studies, at least 7 animals were used per condition for each experimental cohort. We estimated that this would be sufficient to detect a biologically relevant difference in survival, based on the observed variation in tumor progression from previous studies (7, 9). No animals were excluded from analyses. Animals were allocated randomly across different conditions with approximately even distribution based on sex and age.

Generation of Rosa26-CAGGS-LSL-Cas9-GFP-Csy4 Allele. The Rosa26-CAGGS-LSL-Cas9-GFP-Csy4 targeting vector was generated using constructs generated for the Gibson assembly-based modular assembly platform (GMAP) as described previously (62). In brief, the 3xFLAG-NLS-hSpCas9-2A-GFP-2A-Csy4 gene C fragment was cloned into the CAG-driven R26TV LSL backbone targeting vector by Gibson assembly using the conditions described for GMAP.

The assembled Rosa26-CAGGS-LSL-Cas9-GFP-Csy4 targeting vector was linearized by digestion with BsmBI (New England Biolabs). Around 40 μg of the linearized vector was transfected by electroporation into mixed B6;129 embryonic stem cells, followed by selection with 350-μg/mL G418 (Life Technologies) for 7 d. Clones were screened by PCR and sequencing to confirm correct targeting into the *Rosa26* locus, then injected into CD1 donor blastocysts to generate chimeric mice. High-degree chimeric mice were crossed into the *Trp53*$^{flox/flox}$; *Rb1*$^{flox/flox}$; *Rosa26*$^{LSL\text{-}Luciferase/LSL\text{-}Luciferase}$ background to obtain stocks of *Trp53*$^{flox/flox}$; *Rb1*$^{flox/flox}$; *Rosa26*$^{LSL\text{-}Cas9\text{-}GFP\text{-}Csy4/LSL\text{-}Luciferase}$ mice for experiments.

Generation of Ad5-USEC Vectors. To generate a GMAP-compatible adenoviral vector, a filler sequence containing site #1 (GATCAGTGTGAGGGAGTGTAAAGCTGGTTT) and site #5 (AAACGTTGTTGTTTGGGGTTGAATTACTCT) was amplified by PCR using lentiCRISPRv2 (36) as a template and the Ad5-GMAP-filler-F and Ad5-GMAP-filler-R primers, digested with XhoI and EcoRI (New England Biolabs), then ligated into XhoI/EcoRI-digested pacAd5 shuttle vector (63). The resulting vector was linearized with BspEI (New England Biolabs) for subsequent Gibson assembly. Primer sequences are listed in *SI Appendix*, Table S1.

sgRNAs targeting *p107*, *p130*, and a control unannotated region on mouse chromosome 4 were designed using the Broad Institute sgRNA designer tool (64). sgRNA sequences are listed in *SI Appendix*, Table S2. sgRNAs were cloned into lentiCRISPRv2 using the recommended protocol (36). GMAP-compatible U6-sgRNA cloning fragments for each sgRNA were amplified by PCR from the corresponding lentiCRISPRv2-sgRNA vectors using the U6-pA-F and tracrRNA-gA-R primers (*SI Appendix*, Table S1). Ad5-USEC vectors were assembled by Gibson assembly using the BspEI-linearized adenoviral vector, U6-sgRNA cloning fragments, as well as pEFS promoter B and NLS-Cre gene B parts from the GMAP collection (62). All vectors were verified by sequencing before use. Adenoviral vectors were packaged at the Viral Vector Core of the Horae Gene Therapy Center, University of Massachusetts Medical School.

Cell Culture. All cell lines were maintained in DMEM (Corning #10–013-CV) supplemented with 10% FBS, 2-mM L-glutamine (Gibco #25030), and 50-μg/mL gentamicin (Gibco #15710). Lentiviral vectors were generated in HEK293T cells. In brief, cells were plated 1 d before transfection, then cotransfected with lentiviral constructs and packaging plasmids psPAX2 and pMD2.G (Addgenes #12260 and #12259; both plasmids were gifts from Didier Trono). Viral supernatant was harvested 48 and 72 h after transfection, then frozen at −80 °C. Green-Go reporter cells (27) were transduced with lentiCas9-Blast virus (Addgene #52962; plasmid was a gift from Feng Zhang), then selected with 20-μg/mL blasticidin S (Gibco #A11139) for 7 d. All cell lines were tested and found to be negative for mycoplasma contamination before experiments.

Flow Cytometry. Cells were trypsinized, centrifuged at 1,000 rpm (∼200 × g) for 5 min, resuspended in FACS buffer (PBS, 0.5% FBS, 2-mM EDTA), then filtered through a 35-μm cell strainer (Corning #352235). Samples were sorted on a BD FACSAria III system (BD Biosciences).

Immunoblotting. Cells were lysed with RIPA lysis buffer (Thermo Scientific #89900) supplemented with a 1× protease and phosphatase inhibitor mixture (Thermo Scientific #78440), rotated at 4 °C for 30 min, then centrifuged at 13,000 × g for 30 min. Protein concentration was quantified using the bicinchoninic acid assay (Thermo Scientific #23225). Around 40 μg of protein was run on a 4–12% Bis-Tris gradient gel (Invitrogen #NP0335), then transferred onto a nitrocellulose membrane. The following primary antibodies were used for immunoblotting: rabbit anti-p107 (Santa Cruz #sc-318, 1:500), rabbit anti-p130 (Santa Cruz #sc-317, 1:500), and rabbit anti-β-actin (Cell Signaling Technology #4970, 1:10,000). Primary antibodies were detected with the following fluorescent secondary antibodies: IRDye 680RD donkey anti-rabbit IgG (LI-COR #926–68073, 1:10,000), IRDye 800CW donkey anti-rabbit IgG (LI-COR # 926–32,213, 1:10,000). Immunoblots were imaged using the LI-COR Odyssey infrared imager and quantified using Image Studio (LI-COR).

Genomic DNA Isolation and Deep Sequencing of Target Loci. Tumor tissues were dissected from lungs, lymph nodes, or liver tissue upon necropsy, snap-frozen in liquid nitrogen, then stored at −80 °C until subsequent processing. Genomic DNA was isolated from tumors using the Gentra PureGene tissue kit (QIAGEN #158667). Genomic loci were amplified by PCR using either Herculase II Fusion DNA Polymerase (Agilent #600675) for control sgRNA samples or KAPA HiFi DNA polymerase (KAPA Biosystems #KK2601) for sgp107 and sgp130 samples. Primer sequences are listed in *SI Appendix*, Table S3. Amplified samples were purified using the QIAquick PCR purification kit

Downloaded at MIT LIBRARIES on March 30, 2020

(QIAGEN #28104), then submitted for deep sequencing using the CRISPR sequencing service at the DNA Core of the Center for Computational & Integrative Biology (CCIB), Massachusetts General Hospital. Sequence variant detection was performed by the CCIB DNA Core using their standard algorithm.

RNA Isolation and RNA Sequencing. Snap-frozen tumors stored at −80 °C were disrupted and homogenized using the Geno/Grinder (SPEX SamplePrep), then total RNA and genomic DNA were isolated using the AllPrep DNA/RNA mini kit (QIAGEN #80204). RNA samples were submitted for sequencing library preparation by the MIT BioMicro Center using the KAPA mRNA hyperprep kit, and RNA-seq was performed on an Illumina HiSeq 2000 system (40-nt single-end reads).

Gene Expression Signature Analyses. Illumina HiSeq 2000 40-base single-end reads were mapped to the UCSC mm9 mouse genome build (http://genome.ucsc.edu/) using Bowtie (65), and expression counts were quantified using RSEM (66). Raw estimated expression counts were upper-quartile normalized to a count of 1,000 (67). Genes with low normalized counts (upper quartile of a gene's expression across all samples <20) were filtered out as lowly expressed and eliminated from further analyses.

A high-resolution signature discovery approach, independent component analysis (ICA), was employed to characterize global gene expression profiles, as described previously (68–72). This unsupervised blind source separation technique was used on this discrete count-based expression dataset to elucidate statistically independent and biologically relevant signatures. ICA is a signal processing and multivariate data analysis technique in the category of unsupervised matrix factorization methods. Conceptually, ICA decomposes the overall expression dataset into independent signals (gene expression patterns) that represent distinct signatures. High-ranking positively and negatively correlated genes in each signature represent gene sets that drive the corresponding expression pattern (in either direction). Each signature is, thus, 2 sided, allowing for identification of up-regulated and down-regulated genes for each signature within each sample. Formally, utilizing input data consisting of a genes-samples matrix, ICA uses higher order moments to characterize the dataset as a linear combination of statistically independent latent variables. These latent variables represent independent components based on maximizing non-Gaussianity and can be interpreted as independent source signals that have been mixed together to form the dataset under consideration. Each component includes a weight assignment to each gene that quantifies its contribution to that component (signature or latent variable matrix). Additionally, ICA derives a mixing matrix that describes the contribution of each sample toward the signal embodied in each component. This mixing matrix can be used to select signatures among components with distinct gene expression profiles across the set of samples. The R implementation of the core joint approximate diagonalization of eigenmatrices (JADE) algorithm (73–75) was used along with custom R utilities. Signatures were visualized using the Hinton diagram (R plotrix library), and statistical significance of biologically relevant signatures was assessed using the Mann–Whitney–Wilcoxon test ($\alpha = 0.05$).

Initial signature analysis with all chromosomes detected a strong gender-based signature reflecting the known gender bias within the sample set. Subsequent analysis was restricted to autosomes and detected a biologically relevant (sgp107 vs. sgp130) statistically significant ($P = 0.0104$) signature, which was used for downstream enrichment analysis.

All RNA-seq analyses were conducted in the R Statistical Programming language (http://www.r-project.org/). GSEA was carried out using the preranked mode with default settings (39).

Histology and Immunohistochemistry (IHC). Harvested tissues were fixed with zinc formalin (Polysciences #21516) overnight at room temperature, then transferred to 70% ethanol until subsequent paraffin embedding. H&E staining was performed on 4-μm tissue sections using the Varistain Gemini ES Automated Slide Stainer (Thermo Shandon).

For IHC staining, antigen retrieval was performed in sodium citrate buffer (10 mM, pH 6.0) at 125 °C for 5 min. Endogenous peroxidase activity was blocked at room temperature for 30 min using the Dako dual endogenous enzyme block (Dako #S2003). Slides were stained using the ImmPRESS HRP anti-rabbit IgG (peroxidase) polymer detection kit (Vector Laboratories #MP-7401), the ImmPRESS HRP anti-rat IgG, mouse adsorbed (peroxidase) polymer detection kit (Vector Laboratories #MP-7444), or the mouse on mouse ImmPRESS HRP (peroxidase) polymer kit (Vector Laboratories #MP-2400). The following primary antibodies were used: antiphosphohistone H3 (Ser10; Cell Signaling Technology #9701, 1:200), anti-CC3 (Asp175; Cell Signaling Technology #9661, 1:200), anti-Ascl1/Mash1 (BD Biosciences #556604, 1:200), anti-CGRP (Sigma-Aldrich #C8198, 1:2,500), anti-Hes1 (D6P2U; Cell Signaling Technology #11988, 1:200), anti-CD45 (Abcam #ab10558, 1:1,000), anti-CD3 (Cell Marque #103A-7, 1:200), and anti-CD45R/B220 (RA3-6B2; BioLegend #103201, 1:100). The staining was visualized with DAB (Vector Laboratories #SK-4100), and slides were counterstained with hematoxylin.

Tumor Burden Analysis and IHC Quantification. H&E-stained and IHC-stained slides were imaged using the Aperio AT2 slide scanner (Leica Biosystems) and visualized using either Aperio ImageScope (Leica Biosystems) or QuPath (76). Tumor regions and total lung area were outlined and quantified in either ImageScope or QuPath. Tumor burden was calculated as the percentage of tumor area over the total lung area as measured from the largest cross-sectional region of the lung lobes. Quantification of pHH3 and CC3-positive cells was performed using the positive cell detection analysis tool in QuPath. All analyses were performed in a blinded fashion with the investigator being unaware of the experimental condition while outlining tumor regions for each slide.

Statistical Analyses. All statistical tests were performed using Prism software version 7.02 (GraphPad). P values for comparisons between 2 groups (in Figs. 2–5 and *SI Appendix*, Figs. S3 and S5) were determined by the 2-tailed Student's t test. Outlier analysis (in Fig. 3*D*) was performed using the Grubbs' test with a significance level of 0.001. P values for survival analyses (in Fig. 2*C*) were determined by the log-rank (Mantel–Cox) test. P values for contingency tables (in Fig. 3*E*) were determined by Fisher's exact test. For all statistical tests, a P value of <0.05 was used to denote statistical significance. All error bars denote the SD except for Fig. 2*B* where error bars denote 95% CI.

ACKNOWLEDGMENTS. We thank Wen Xue (University of Massachusetts Medical School) for assistance with packaging adenoviral vectors as well as past and present members of the Jacks Laboratory, particularly Francisco Sánchez-Rivera, Rodrigo Romero, Santiago Naranjo, Tuomas Tammela, Leanne Li, and Caterina Colón for helpful discussions and technical advice. We thank the Koch Institute Swanson Biotechnology Center for technical support, specifically the Animal Imaging & Preclinical Testing Core Facility, the Flow Cytometry Core Facility, and the Hope Babette Tang (1983) Histology Facility. This work was supported by the Howard Hughes Medical Institute, the Ludwig Center for Molecular Oncology at MIT, and, in part, by the Koch Institute Support (core) Grant P30-CA14051 from the National Cancer Institute. S.R.N. was supported by the A*STAR (Agency for Science, Technology and Research, Singapore) National Science Scholarship and the MIT School of Science Fellowship in Cancer Research. T.J. is a Howard Hughes Medical Institute Investigator, the David H. Koch Professor of Biology, and a Daniel K. Ludwig Scholar at MIT.

1. R. Govindan *et al*., Changing epidemiology of small-cell lung cancer in the United States over the last 30 years: Analysis of the surveillance, epidemiologic, and end results database. *J. Clin. Oncol.* **24**, 4539–4544 (2006).
2. R. Califano, A. Z. Abidin, R. Peck, C. Faivre-Finn, P. Lorigan, Management of small cell lung cancer: Recent developments for optimal care. *Drugs* **72**, 471–490 (2012).
3. I. K. Demedts, K. Y. Vermaelen, J. P. van Meerbeeck, Treatment of extensive-stage small cell lung carcinoma: Current status and future prospects. *Eur. Respir. J.* **35**, 202–215 (2010).
4. L. A. Byers, C. M. Rudin, Small cell lung cancer: Where do we go from here? *Cancer* **121**, 664–672 (2015).
5. J. George *et al*., Comprehensive genomic profiles of small cell lung cancer. *Nature* **524**, 47–53 (2015).
6. I. I. Wistuba, A. F. Gazdar, J. D. Minna, Molecular genetics of small cell lung carcinoma. *Semin. Oncol.* **28** (suppl. 4), 3–13 (2001).
7. R. Meuwissen *et al*., Induction of small cell lung cancer by somatic inactivation of both Trp53 and Rb1 in a conditional mouse model. *Cancer Cell* **4**, 181–189 (2003).
8. B. E. Schaffer *et al*., Loss of p130 accelerates tumor development in a mouse model for human small-cell lung carcinoma. *Cancer Res.* **70**, 3877–3883 (2010).
9. D. G. McFadden *et al*., Genetic and clonal dissection of murine small cell lung carcinoma progression by genome sequencing. *Cell* **156**, 1298–1311 (2014).
10. M. Cui *et al*., PTEN is a potent suppressor of small cell lung cancer. *Mol. Cancer Res.* **12**, 654–659 (2014).
11. I. J. Huijbers *et al*., Rapid target gene validation in complex cancer mouse models using re-derived embryonic stem cells. *EMBO Mol. Med.* **6**, 212–225 (2014).
12. A. L. Dooley *et al*., Nuclear factor I/B is an oncogene in small cell lung cancer. *Genes Dev.* **25**, 1470–1475 (2011).
13. S. K. Denny *et al*., Nfib promotes metastasis through a widespread increase in chromatin accessibility. *Cell* **166**, 328–342 (2016).
14. E. A. Semenova *et al*., Transcription factor NFIB is a driver of small cell lung cancer progression in mice and marks metastatic disease in patients. *Cell Rep.* **16**, 631–643 (2016).

Downloaded at MIT LIBRARIES on March 30, 2020

15. N. Wu *et al*., NFIB overexpression cooperates with Rb/p53 deletion to promote small cell lung cancer. *Oncotarget* **7**, 57514–57524 (2016).
16. G. Mollaoglu *et al*., MYC drives progression of small cell lung cancer to a variant neuroendocrine subtype with vulnerability to aurora kinase inhibition. *Cancer Cell* **31**, 270–285 (2017).
17. D. Jia *et al*., *Crebbp* loss drives small cell lung cancer and increases sensitivity to HDAC inhibition. *Cancer Discov.* **8**, 1422–1437 (2018).
18. B. Vogelstein *et al*., Cancer genome landscapes. *Science* **339**, 1546–1558 (2013).
19. M. S. Lawrence *et al*., Mutational heterogeneity in cancer and the search for new cancer-associated genes. *Nature* **499**, 214–218 (2013).
20. M. Peifer *et al*., Integrative genome analyses identify key somatic driver mutations of small-cell lung cancer. *Nat. Genet.* **44**, 1104–1110 (2012).
21. C. M. Rudin *et al*., Comprehensive genomic analysis identifies SOX2 as a frequently amplified gene in small-cell lung cancer. *Nat. Genet.* **44**, 1111–1116 (2012).
22. M. Jinek *et al*., RNA-programmed genome editing in human cells. *eLife* **2**, e00471 (2013).
23. L. Cong *et al*., Multiplex genome engineering using CRISPR/Cas systems. *Science* **339**, 819–823 (2013).
24. P. Mali *et al*., RNA-guided human genome engineering via Cas9. *Science* **339**, 823–826 (2013).
25. W. Xue *et al*., CRISPR-mediated direct mutation of cancer genes in the mouse liver. *Nature* **514**, 380–384 (2014).
26. D. Maddalo *et al*., In vivo engineering of oncogenic chromosomal rearrangements with the CRISPR/Cas9 system. *Nature* **516**, 423–427 (2014).
27. F. J. Sánchez-Rivera *et al*., Rapid modelling of cooperating genetic events in cancer through somatic genome editing. *Nature* **516**, 428–431 (2014).
28. R. J. Platt *et al*., CRISPR-Cas9 knockin mice for genome editing and cancer modeling. *Cell* **159**, 440–455 (2014).
29. L. E. Dow *et al*., Inducible in vivo genome editing with CRISPR-Cas9. *Nat. Biotechnol.* **33**, 390–394 (2015).
30. S.-H. Chiou *et al*., Pancreatic cancer modeling using retrograde viral vector delivery and in vivo CRISPR/Cas9-mediated somatic genome editing. *Genes Dev.* **29**, 1576–1585 (2015).
31. J. Roper *et al*., In vivo genome editing and organoid transplantation models of colorectal cancer and metastasis. *Nat. Biotechnol.* **35**, 569–576 (2017).
32. J. Huang *et al*., Generation and comparison of CRISPR-Cas9 and Cre-mediated genetically engineered mouse models of sarcoma. *Nat. Commun.* **8**, 15999 (2017).
33. R. E. Haurwitz, M. Jinek, B. Wiedenheft, K. Zhou, J. A. Doudna, Sequence- and structure-specific RNA processing by a CRISPR endonuclease. *Science* **329**, 1355–1358 (2010).
34. L. Nissim, S. D. Perli, A. Fridkin, P. Perez-Pinera, T. K. Lu, Multiplexed and programmable regulation of gene networks with an integrated RNA and CRISPR/Cas toolkit in human cells. *Mol. Cell* **54**, 698–710 (2014).
35. M. DuPage, A. L. Dooley, T. Jacks, Conditional mouse lung cancer models using adenoviral or lentiviral delivery of Cre recombinase. *Nat. Protoc.* **4**, 1064–1072 (2009).
36. N. E. Sanjana, O. Shalem, F. Zhang, Improved vectors and genome-wide libraries for CRISPR screening. *Nat. Methods* **11**, 783–784 (2014).
37. J. S. Lim *et al*., Intratumoural heterogeneity generated by Notch signalling promotes small-cell lung cancer. *Nature* **545**, 360–364 (2017).
38. A. Hyvärinen, E. Oja, Independent component analysis: Algorithms and applications. *Neural Netw.* **13**, 411–430 (2000).
39. A. Subramanian *et al*., Gene set enrichment analysis: A knowledge-based approach for interpreting genome-wide expression profiles. *Proc. Natl. Acad. Sci. U.S.A.* **102**, 15545–15550 (2005).
40. F. J. Sánchez-Rivera, T. Jacks, Applications of the CRISPR-Cas9 system in cancer biology. *Nat. Rev. Cancer* **15**, 387–395 (2015).
41. L. A. Gilbert *et al*., CRISPR-mediated modular RNA-guided regulation of transcription in eukaryotes. *Cell* **154**, 442–451 (2013).
42. A. Chavez *et al*., Highly efficient Cas9-mediated transcriptional programming. *Nat. Methods* **12**, 326–328 (2015).
43. M. E. Tanenbaum, L. A. Gilbert, L. S. Qi, J. S. Weissman, R. D. Vale, A protein-tagging system for signal amplification in gene expression and fluorescence imaging. *Cell* **159**, 635–646 (2014).
44. S. Konermann *et al*., Genome-scale transcriptional activation by an engineered CRISPR-Cas9 complex. *Nature* **517**, 583–588 (2015).
45. J. E. Dahlman *et al*., Orthogonal gene knockout and activation with a catalytically active Cas9 nuclease. *Nat. Biotechnol.* **33**, 1159–1161 (2015).
46. P. Perez-Pinera *et al*., RNA-guided gene activation by CRISPR-Cas9-based transcription factors. *Nat. Methods* **10**, 973–976 (2013).
47. H.-K. Liao *et al*., In vivo target gene activation via CRISPR/Cas9-mediated trans-epigenetic modulation. *Cell* **171**, 1495–1507.e15 (2017).
48. M. M. Winslow *et al*., Suppression of lung adenocarcinoma progression by Nkx2-1. *Nature* **473**, 101–104 (2011).
49. C. H. Chuang *et al*., Molecular definition of a metastatic lung cancer state reveals a targetable CD109-Janus kinase-Stat axis. *Nat. Med.* **23**, 291–300 (2017).
50. S. H. Chiou *et al*., BLIMP1 induces transient metastatic heterogeneity in pancreatic cancer. *Cancer Discov.* **7**, 1184–1199 (2017).
51. A. McKenna *et al*., Whole-organism lineage tracing by combinatorial and cumulative genome editing. *Science* **353**, aaf7907 (2016).
52. R. Kalhor, P. Mali, G. M. Church, Rapidly evolving homing CRISPR barcodes. *Nat. Methods* **14**, 195–200 (2017).
53. K. L. Frieda *et al*., Synthetic recording and in situ readout of lineage information in single cells. *Nature* **541**, 107–111 (2017).
54. J. R. Nevins, Toward an understanding of the functional complexity of the E2F and retinoblastoma families. *Cell Growth Differ.* **9**, 585–593 (1998).
55. E. J. Smith, G. Leone, J. DeGregori, L. Jakoi, J. R. Nevins, The accumulation of an E2F-p130 transcriptional repressor distinguishes a G0 cell state from a G1 cell state. *Mol. Cell. Biol.* **16**, 6965–6976 (1996).
56. S. E. Wirt, J. Sage, p107 in the public eye: An Rb understudy and more. *Cell Div.* **5**, 9 (2010).
57. D. S. Simpson, N. A. Mason-Richie, C. A. Gettler, K. A. Wikenheiser-Brokamp, Retinoblastoma family proteins have distinct functions in pulmonary epithelial cells in vivo critical for suppressing cell growth and tumorigenesis. *Cancer Res.* **69**, 8733–8741 (2009).
58. N. Hiraoka, Y. Ino, R. Yamazaki-Itoh, Tertiary lymphoid organs in cancer tissues. *Front. Immunol.* **7**, 244 (2016).
59. C. Sautès-Fridman *et al*., Tertiary lymphoid structures in cancers: Prognostic value, regulation, and manipulation for therapeutic intervention. *Front. Immunol.* **7**, 407 (2016).
60. C. D. Buckley, F. Barone, S. Nayar, C. Bénézech, J. Caamaño, Stromal cells in chronic inflammation and tertiary lymphoid organ formation. *Annu. Rev. Immunol.* **33**, 715–745 (2015).
61. Y. Xia *et al*., Targeting CREB pathway suppresses small cell lung cancer. *Mol. Cancer Res.* **16**, 825–832 (2018).
62. E. H. Akama-Garren *et al*., A modular assembly platform for rapid generation of DNA constructs. *Sci. Rep.* **6**, 16836 (2016).
63. R. D. Anderson, R. E. Haskell, H. Xia, B. J. Roessler, B. L. Davidson, A simple method for the rapid generation of recombinant adenovirus vectors. *Gene Ther.* **7**, 1034–1038 (2000).
64. J. G. Doench *et al*., Optimized sgRNA design to maximize activity and minimize off-target effects of CRISPR-Cas9. *Nat. Biotechnol.* **34**, 184–191 (2016).
65. B. Langmead, C. Trapnell, M. Pop, S. L. Salzberg, Ultrafast and memory-efficient alignment of short DNA sequences to the human genome. *Genome Biol.* **10**, R25 (2009).
66. B. Li, C. N. Dewey, RSEM: Accurate transcript quantification from RNA-seq data with or without a reference genome. *BMC Bioinf.* **12**, 323 (2011).
67. J. H. Bullard, E. Purdom, K. D. Hansen, S. Dudoit, Evaluation of statistical methods for normalization and differential expression in mRNA-Seq experiments. *BMC Bioinf.* **11**, 94 (2010).
68. C. M. C. Li *et al*., Foxa2 and Cdx2 cooperate with Nkx2-1 to inhibit lung adenocarcinoma metastasis. *Genes Dev.* **29**, 1850–1862 (2015).
69. N. Dimitrova *et al*., Stromal expression of miR-143/145 promotes neoangiogenesis in lung cancer development. *Cancer Discov.* **6**, 188–201 (2016).
70. T. Papagiannakopoulos *et al*., Circadian rhythm disruption promotes lung tumorigenesis. *Cell Metab.* **24**, 324–331 (2016).
71. R. Romero *et al*., Keap1 loss promotes Kras-driven lung cancer and results in dependence on glutaminolysis. *Nat. Med.* **23**, 1362–1368 (2017).
72. G. Mollaoglu *et al*., The lineage-defining transcription factors SOX2 and NKX2-1 determine lung cancer cell fate and shape the tumor immune microenvironment. *Immunity* **49**, 764–779.e9 (2018).
73. J. Miettinen, K. Nordhausen, S. Taskinen, Blind source separation based on joint diagonalization in R: The packages JADE and BSSasymp. *J. Stat. Softw.*, 10.18637/jss.v076.i02 (2017).
74. D. N. Rutledge, D. Jouan-Rimbaud Bouveresse, Independent components analysis with the JADE algorithm. *TrAC Trends Analyt. Chem.* **50**, 22–32 (2013).
75. A. Biton *et al*., Independent component analysis uncovers the landscape of the bladder tumor transcriptome and reveals insights into luminal and basal subtypes. *Cell Rep.* **9**, 1235–1245 (2014).
76. P. Bankhead *et al*., QuPath: Open source software for digital pathology image analysis. *Sci. Rep.* **7**, 16878 (2017).

Downloaded at MIT LIBRARIES on March 30, 2020